LETTERS
PUBLISHED ONLINE: 29 AUGUST 2010 | DOI: 10.1038/NPHOTON.2010.205
nature photonics

Ultrafast Rabi flopping and coherent pulse propagation in a quantum cascade laser

Hyunyong Choi[1,2†], Vasileios-Marios Gkortsas[3†], Laurent Diehl[4], David Bour[5], Scott Corzine[5], Jintian Zhu[5], Gloria Höfler[5], Federico Capasso[4], Franz X. Kärtner[3*] and Theodore B. Norris[1*]

Pulse propagation phenomena are central to ultrashort pulse generation and amplification in lasers[1–5]. In the coherent regime, the phase relationship between the pulse and the material transition is preserved, allowing both optical fields and material states to be controlled[6]. The most prominent form of coherent manipulation is Rabi flopping[7], a phenomenon well established in few-level absorbers, including atoms and single quantum dots[8–19]. However, Rabi flopping is generally much weaker in semiconductors because of strong dephasing in the electronic bands, in contrast to discrete-level systems. Although low-density induced coherent oscillations have been observed in semiconductor absorbers[11,13–20], coherent pulse propagation phenomena in active semiconductor devices have not been observed. In this Letter, we explore coherent pulse propagation in an operating quantum cascade laser and directly observe Rabi flopping and coherent pulse reshaping. This work demonstrates the applicability of few-level models for quantum cascade lasers and may stimulate novel approaches to short pulse generation[21,22].

In the coherent light–matter interaction regime, an ultrashort pulse (a pulse with a duration shorter than the dephasing time) incident on a two-level absorber can drive coherent Rabi oscillations of the population if the pulse area is on the order of or greater than π. If the absorbing medium is optically thick, coherent interaction leads to pulse reshaping and the McCall–Hahn area theorem[23]. The interaction strength is characterized by the Rabi flopping frequency Ω_R, which is linearly proportional to the dipole moment and the electric field strength[24]. Rabi oscillation relies on the coherent interaction of a pulse with an appropriately narrow optical resonance, that is, when Ω_R exceeds the dephasing rate of the transition[24]. In semiconductors, therefore, Rabi flopping is usually hindered due to the lack of a narrow resonance for interband transitions (due to the opposite curvature of the electronic bands), or to excitation-induced phase-breaking processes on excitonic transitions, which can occur on subpicosecond timescales, several orders of magnitude shorter than in typical atomic systems[17]. For these reasons, although there have been predictions of Rabi oscillations in semiconductor amplifiers[4], to date there have been no time-resolved reports of coherent pulse propagation and reshaping.

Intersubband transitions in semiconductor quantum heterostructures, on the other hand, have parallel subbands and therefore behave quite similarly to discrete-level systems. In addition, intersubband transitions afford the possibility of engineering very high dipole moments[25], thus providing a promising laboratory for the study of coherent interactions. Recent studies of quantum cascade lasers (QCLs) exhibiting coherent instabilities have suggested the possibility of population modulations, manifested as sidebands in the output spectrum that scale linearly with the intracavity optical field[5]. The population dynamics, however, is in a small-signal regime with modulation of a few percent. These observations have motivated the use of direct time-resolved techniques to explore the large-signal dynamics of Rabi flopping and its impact on coherent pulse propagation phenomena.

Our approach to the problem is to measure the time evolution of the transient laser output following ultrashort resonant pulse injection into an operating QCL[26] (see Methods). The low-temperature *L–I* characteristic of the QCL is shown in Fig. 1a. This QCL shows significant spectral broadening above threshold, stemming from multimode instabilities such as spatial hole burning and the Risken–Nummedal–Graham–Haken instability[5]. A schematic of our experiment is shown in Fig. 1b, in which a femtosecond Ti:Sapphire laser system (Coherent RegA) is used to generate mid-infrared (mid-IR) pulses through optical parametric amplification (OPA) and difference frequency generation (DFG)[26]. The OPA/DFG system is tuned so that the pulse spectrum overlaps the QCL gain transition. As shown in Fig. 1c, the bandwidth of the mid-IR pulse (red) is larger than the QCL lasing spectrum (blue), and is almost as broad as the electroluminescence (EL) spectrum (black) of the QC structure. The 150-fs mid-IR pulses are injected into the QCL waveguide, and the light exiting the end facet after traversing the cavity is collected and focused into a nonlinear KTA($KTiOAsO_4$) crystal together with 120-fs 800-nm probe pulses from the Ti:Sapphire amplifier. The sum frequency of the QCL output and the 800-nm probe pulse is detected using a photomultiplier tube (PMT), and the time delay between the probe and mid-IR pulses is varied to give the complete time evolution of the QCL output before, during and after pulse injection. Figure 1d shows a typical cross-correlation of the probe and QCL output following pump-pulse injection. A time-zero reference is provided by cross-correlation of a portion of the mid-IR pulse not coupled into the QCL. A pulse coupled into the QCL arrives at a time corresponding to a transit delay through the cavity. Subsequent pulses are observed at delays corresponding to integer numbers of roundtrips.

The main experimental observations are presented in Fig. 2 for injected pulse areas Θ_{in} of approximately π, 2π and 3π (see Methods). At negative delay before pulse injection, the upconverted signal is constant, as the QCL is biased above threshold. The injected pulse shows some broadening due to dispersion[26] at a low Θ_{in} of π (Fig. 2a). As Θ_{in} increases, the pulse peak advances to earlier timepoints; for 2π this advance in time is 38 fs (Fig. 2b), becoming as large as 81 fs for Θ_{in} approaching 3π (Fig. 2c). The pulse is also

[1]Center for Ultrafast Optical Science and Department of Electrical Engineering and Computer Science, University of Michigan, Ann Arbor, Michigan 48109-2099, USA, [2]Materials Sciences Division, Lawrence Berkeley National Laboratory, Berkeley, California 94720, USA, [3]Research Laboratory of Electronics and Department of Electrical Engineering and Computer Science, Massachusetts Institute of Technology, Cambridge, Massachusetts 02139, USA, [4]School of Engineering and Applied Sciences, Harvard University, Cambridge, Massachusetts 02138, USA, [5]Agilent Laboratories, 3500 Deer Creek Road, Palo Alto, California 94304, USA; †These authors contributed equally to this work. *e-mail: kaertner@mit.edu; tnorris@eecs.umich.edu

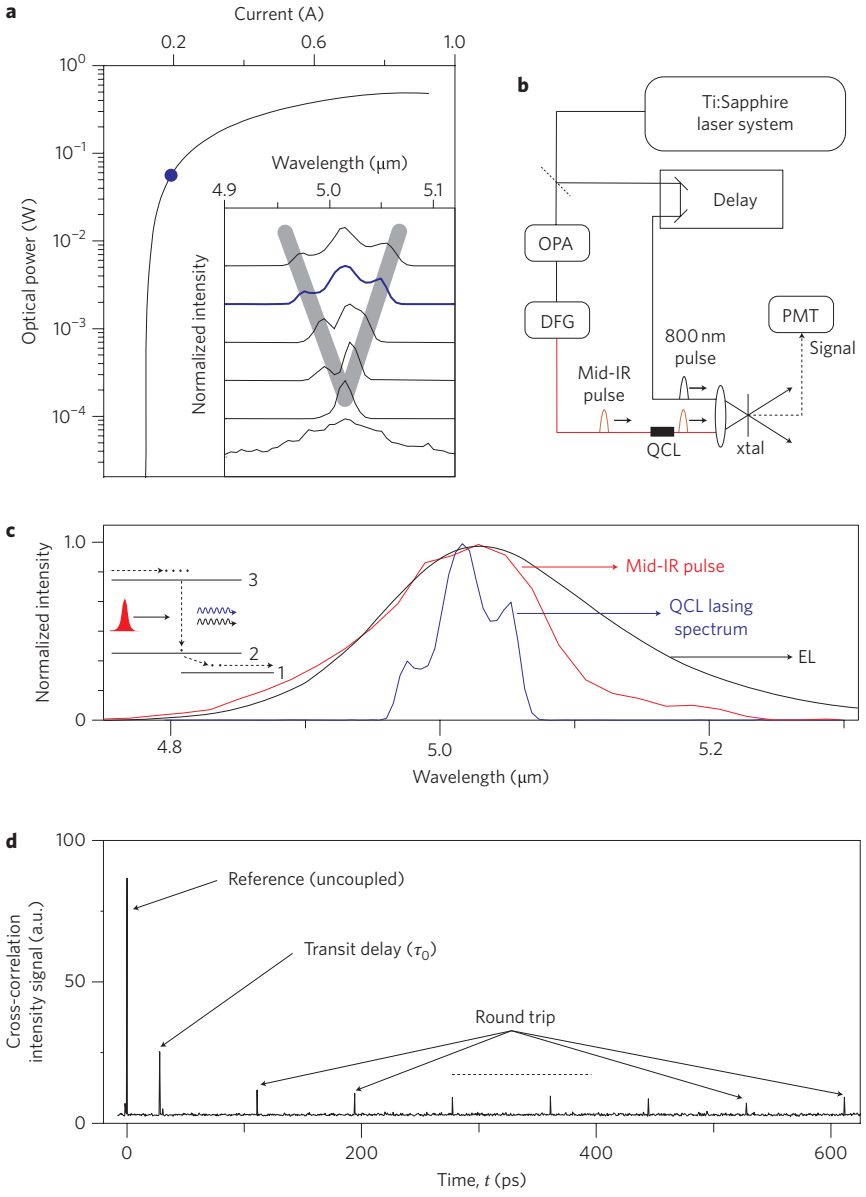

Figure 1 | Experimental scheme. a, Low-temperature light versus current (L–I) characteristics (at 30 K) of the QCL used in this study. The c.w. emission spectra are shown in the inset, from below threshold to above threshold. The spectrum taken for this measurement is shown as a thick blue curve (1.5 times above threshold is marked as a blue dot in the L–I curve). **b**, Schematic set-up of the ultrafast time-resolved cross-correlation measurement using a 250-kHz Ti:Sapphire regenerative amplifier laser system. The mid-IR pulses are generated via optical parametric amplification (OPA) and difference frequency generation (DFG). The sum-frequency signal of the QCL output and an 800-nm pulse is detected using a photomultiplier tube (PMT). Xtal is nonlinear KTA crystal. **c**, Normalized mid-IR pulse and QCL lasing spectrum with an electroluminescence (EL) spectrum of the QC structure, taken from the same wafer (D3281). A Lorentzian fit to this EL yields a dephasing rate $1/T_2'$ of 0.08 ps^{-1} (as discussed in ref. 26). **d**, Typical cross-correlation signal when the QCL is biased near threshold. An uncoupled mid-IR pulse (for example, through the QCL waveguide cladding) is used as a reference time-zero delay. Once the pulse is coupled, the propagating pulse experiences a transit delay and several roundtrip delays. In this work, we focus on the dynamics at the transit delay. The estimated coupling efficiency is ~0.2%, from a measured mid-IR pulse spot diameter of 70 μm and QCL facet area of 7.5 μm × 1 μm. All measurements were performed at a QCL bias of 1.5 times above threshold and at a cold finger temperature of 30 K.

reshaped, with indications of the onset of pulse breakup. In Fig. 2g, the signal scale is expanded to investigate the effect of gain saturation in more detail. Following the pulse, it can be clearly seen that the laser intensity is suppressed by as much as ~60% (compared to the lasing intensity before the pulse) when Θ_{in} is π (black curve) and 2π (red curve); this is due to saturation of the gain by the injected pulse. The QCL output recovers to its steady-state level with a time constant of ~1 ps, close to the gain recovery time due to transport in the QCL[27].

The key observation, however, is that when Θ_{in} approaches 3π, there is no significant saturation of the lasing intensity (blue curve in Fig. 2g). In other words, for this pulse area, there is no apparent reduction in gain following the injected pulse. This is directly analogous to the reduction in absorption of a pulse propagating in an absorbing medium as the area approaches 2π, leading to self-induced transparency[23]. Whereas incoherent saturation of the gain would lead to gain saturation increasing monotonically with pulse area, the signature of coherent pulse propagation and Rabi flopping is the coherent re-establishment of the gain by the trailing edge of the pulse. Of course, one would intuitively expect the coherent re-establishment of the gain to occur in a two-level system for a pulse area

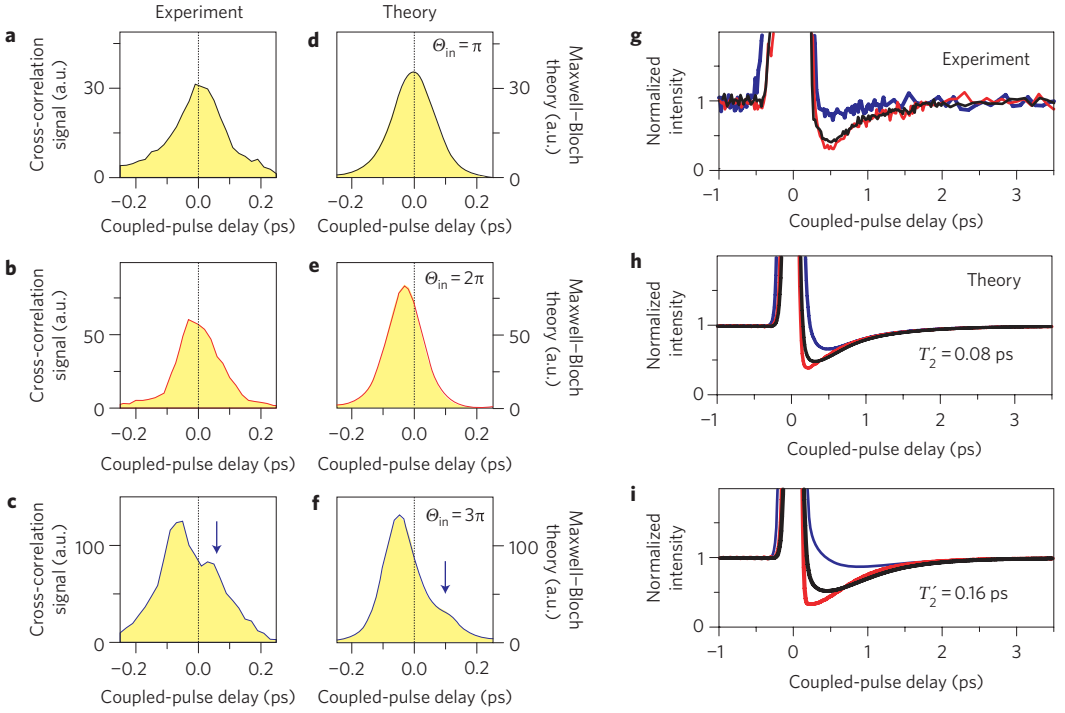

Figure 2 | Pulse envelope and lasing dynamics. a, For an injected pulse area Θ_{in} of π (the corresponding mid-IR pulse intensity in the QCL is $\sim 4.6 \times 10^7$ W cm^{-2}), no discernable time shift or envelope distortion are observed. **b**, When Θ_{in} increases to 2π ($\sim 1.6 \times 10^8$ W cm^{-2}), the peak envelope is shifted to an earlier time, with some pulse reshaping. **c**, Further increasing Θ_{in} towards 3π ($\sim 3.4 \times 10^8$ W cm^{-2}) results in a significant time shift and envelope distortion (blue arrow). For direct comparison, all curves are plotted versus the coupled-pulse delay; the transit delay (τ_0) is subtracted from the 800-nm probe delay time (t). **d**, Maxwell–Bloch simulation results for Θ_{in} is π. **e**, Increasing Θ_{in} to 2π results in a time advance of the envelope peak. **f**, When Θ_{in} reaches 3π, both the time advance of the envelope peak and a significantly distorted pulse envelope (blue arrow) are clearly visible. **g**, Measured lasing dynamics when Θ_{in} is π (black), 2π (red) and 3π (blue). **h**,**i**, Simulated lasing dynamics when Θ_{in} is π (black), 2π (red) and 3π (blue), with T_2' equal to 80 fs (**h**) and 160 fs (**i**). All curves shown in Fig. 2 are normalized to the QCL steady-state lasing intensity, and the simulation results are convolved with a 150-fs-long Gaussian pulse.

of 2π. Hence, to understand the experimental results quantitatively, it is necessary to develop a realistic model of the pulse propagation, incorporating dephasing and the three-level nature of the QCL system.

The Maxwell–Bloch equations provide a framework for modelling the coherent interaction of short pulses and few-level systems, including the effects of propagation on pulse evolution[1]. Although a two-level model may be sufficient to demonstrate the observed behaviour qualitatively, it has been well established by the design and characterization of the QCL under consideration (and by our previous time-resolved gain dynamics experiments[28]) that it operates as a three-level system. The three-level Maxwell–Bloch equations in the slowly varying envelope approximation are given as[29]

$$\partial_t \eta = \frac{i}{2}(\rho_3 - \rho_2)E - \frac{\eta}{T_2'}$$

$$\partial_t \rho_3 = \lambda + \frac{i}{2}(E^*\eta - \eta^* E) - \frac{\rho_3}{T_{32}}$$

$$\partial_t \rho_2 = -\frac{i}{2}(E^*\eta - \eta^* E) - \frac{\rho_2}{T_{21}} + \frac{\rho_3}{T_{32}}$$

$$\partial_t \rho_1 = -\lambda + \frac{\rho_2}{T_{21}}$$

$$\frac{n}{c}\partial_t E + \partial_z E = -\frac{i\omega N d^2}{\hbar \varepsilon_0 c n}\eta - \frac{l_{loss}}{2}E$$

where E and η are the envelope of the electric field and the polarization, ρ_3, ρ_2 and ρ_1 are the occupation probabilities of each level, d is the dipole matrix element (1.6e nm, calculated) and l_{loss} is the effective cavity loss (4 cm^{-1}, assumed). T_{32} and T_{21} are the lifetimes of level 3 (1 ps, assumed) and level 2 (0.2 ps, assumed), T_2' is the dephasing time (0.08 ps, measured[26]) and λ is a pumping term (1.5 times above threshold). N and n are the electron density and refractive index (3.5, assumed).

The numerical simulation results using these Maxwell–Bloch equations are presented in Fig. 2 ('Theory') and are directly compared with the experimental results. For the envelopes of the propagated pulses (Fig. 2d–f), the advance of the pulse maxima agrees very well with experimental findings. The reshaping of the pulse envelope is also clearly visible when Θ_{in} approaches 3π (blue arrow in Fig. 2f).

The experimentally observed suppression of laser intensity immediately following pulse injection (Fig. 2g) is qualitatively reflected in the simulations (Fig. 2h,i). There is a consistent trend in which the magnitude of the laser suppression increases as Θ_{in} increases from π to 2π, and becomes weaker when Θ_{in} is 3π, in agreement with experiment. The precise amount of suppression after pulse injection as a function of Θ_{in} strongly depends on the dephasing time T_2' used in the model. Figure 2h and i shows results comparing T_2' of 80 and 160 fs. Clearly, for longer T_2', excellent agreement between theory and experiment can be obtained; the measured EL spectrum may be broader than the expected T_2' of 160 fs due to inhomogeneous broadening.

By examining the results of the simulation for the population inversion and polarization between levels 3 and 2, we can gain considerable insight into the coherent interaction of the gain medium

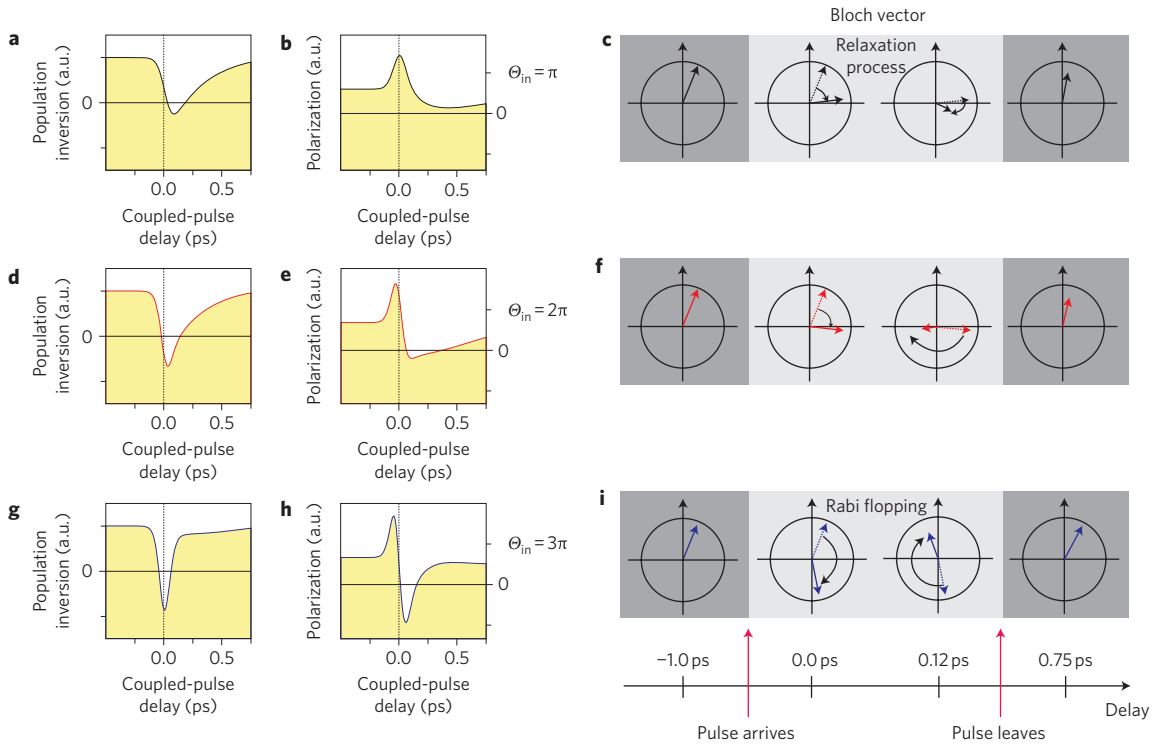

Figure 3 | Dynamics of population inversion and polarization, and Bloch vectors. a–c, When Θ_{in} is π, population inversion (**a**), polarization (**b**) and the corresponding Bloch vector rotation (**c**) follow an incoherent 'relaxation process' (for explanation see text). In this case, Ω_R (8.3 THz) is smaller than $1/T_2'$ (12.5 THz, $T_2' = 80$ fs). **d–f**, Increasing Θ_{in} to 2π results in an intermediate behaviour between incoherent and coherent dynamics, as seen in the inversion (**d**), polarization (**e**) and Bloch vector rotation (**f**). In this limit, Ω_R (16.7 THz) is slightly larger than $1/T_2'$. **g**, When Θ_{in} is 3π, inversion saturation advances to earlier times as a result of gain extraction, and the suppressed gain is coherently re-pumped at the trailing edge of the pulse. **h**, The polarization shows a clear sign reversal on the trailing edge of the pulse, corresponding to coherent repumping of the gain. **i**, The corresponding Bloch vector continues its rotation during pulse transit due to coherent Rabi flopping. In this limit, Ω_R (20.9 THz) is much larger than $1/T_2'$. The estimated Rabi frequency Ω_R is calculated for the coupled-pulse delay when the pulse area Θ_{in} (π, 2π and 3π) is used as an input pulse in the Maxwell–Bloch equations.

and the propagating pulse. Figure 3 shows the calculated inversion and polarization, as well as a schematic of the corresponding Bloch vector. It should be noted that the length of the Bloch vector is not conserved and the tipping angle does not correspond directly to the pulse area as in a closed two-level system, because levels 3 and 2 are coupled to level 1 through relaxation. The Bloch vector initially points 'north', but with a small nonzero steady-state polarization due to the continuous-wave (c.w.) QCL field. (In general, the phase of the oscillating QCL field will be random with respect to that of the injected pulse, so for simplicity we show only one possible initial phase. In principle one would have to average over all possible phases, but this does not lead to a significant change in the observed dynamics.) Note that Θ_{in} refers to the pulse area inside the input end of the QCL. The injected pulse suffers a net linear attenuation during propagation of a factor of ~4, because it cannot extract enough gain from the QCL to overcome waveguide losses.

For small Θ_{in} (up to about π), the population inversion saturates with the integral of the envelope of the arriving pulse, and recovers after the pulse departs (Fig. 3a) due to electronic transport coupled to level 1. The inversion is driven slightly negative by the pulse, but there is almost no coherent recovery of the gain in the trailing edge of the pulse, and the gain recovery is relatively long due to T_{32}. The corresponding Bloch vector motion (Fig. 3c) is a rotation to the south followed by a slower recovery back to its original steady-state position as the QCL population inversion returns to equilibrium.

For $\Theta_{in} = 3\pi$, the inversion is driven to strongly negative values by the leading edge of the pump pulse, reaching a minimum at the pulse peak (Fig. 3g). At the same time, the polarization is driven to zero (Fig. 3h), so the Bloch vector points straight towards the south at the peak of the pulse (Fig. 3i). During the trailing half of the pulse, the inversion coherently recovers towards its initial value, and the polarization is negative, indicating that the Bloch vector continues to rotate in the same direction towards the north. This coherent recovery of the gain due to the phase shift between the incident pulse and the polarization is precisely analogous to the process leading to self-induced transparency in absorbing media[23]. Because the gain is almost fully restored by the coherent interaction of the pulse and the medium, the QCL output following the pulse is almost unaffected by the passage of the pulse (Fig. 2g, blue). Because the rising edge of the pulse sees gain, while the trailing edge is absorbed, the pulse peak shifts to earlier times[4], as can be observed in Fig. 2c,f. For $\Theta_{in} = 2\pi$ (Fig. 3d–f), the behaviour lies intermediate between the predominantly incoherent response observed for $\Theta_{in} = \pi$ and the almost fully coherent behaviour for $\Theta_{in} = 3\pi$.

It is important to note that, due to the aforementioned losses, the pulse area decreases by nearly a factor of two in propagating along the length of the cavity. Hence, for an input area of 3π, the output area is close to 1.5π; this explains why the observed maximum coherent gain recovery occurs for an input area of 3π instead of 2π; the observed recovery is the result of averaging over the length of the waveguide. This was verified by examining the simulated population behaviour at the input end of the QCL, where a full Bloch vector rotation is found for the expected area of 2π.

In summary, these experiments provide compelling evidence that coherent Rabi oscillation of the gain can be observed in an operating QCL, with very large modulation of the gain and significant propagation-induced coherent reshaping of the pulse. Although the

observed dynamics may be reproduced qualitatively by a two-level model, we have found good quantitative agreement of the QCL output and pulse intensity using the three-level Maxwell–Bloch equations. Looking to the future, it is interesting to note that the fluence of a few-π pulse can be comparable to the fluence corresponding to one roundtrip of a c.w. QCL, suggesting that coherent pulse propagation could play a role in mode-locking[21,22,30] or other schemes for pulse generation.

Methods

QCL. As discussed in ref. 26, the active region of the QCL (D3281) was based on a so-called 'bound-to-continuum' design grown by metal–organic vapour-phase epitaxy. Strained $In_{0.6}Ga_{0.4}As/In_{0.44}Al_{0.56}As$ layers were deposited at a slow rate (0.1 nm s^{-1}), and the doping in the injector region was kept low to limit waveguide losses. The waveguide consisted of two low-doped InGaAs layers (thickness, 300 nm; doping, 3×10^{16} cm^{-3}) and two InP cladding layers (thickness, 3 μm; doping, 1×10^{17} cm^{-3}) surrounding the 30 QCL stacks comprising the waveguide core. A highly doped InP cap layer (thickness, 0.5 μm; doping, 1×10^{19} cm^{-3}) was grown to decouple the optical mode from the lossy metal contacts. The QCL device was a buried heterostructure laser with Fe-doped InP regrown on the side of the ridge. The ridge width of the studied QCL was 7.5 μm and its length ~3.7 mm.

Pulse area in the QCL. The injected pulse intensity into the QCL (and the corresponding pulse area Θ_{in}) was estimated using the following steps. The measured input mid-IR pulse intensity I_{in} was used to estimate the output mid-IR pulse intensity I_{out} by taking into account the following series of losses: coupling efficiency η_c of 0.2%, QCL reflection loss l_r of 31%, effective waveguide loss l_{loss} of 4 cm^{-1}, QCL transmission loss l_t of 69%, cryostat window loss l_c of 3% (×2) and collection efficiency loss l_{ce} of 50%. I_{out} was then estimated by comparing the measured cross-correlation ratio to the QCL lasing intensity. Finally, the injected pulse intensity into the QCL was used as an initial condition for the Maxwell–Bloch equations (with a loss l_{loss} of 4 cm^{-1}), and the simulation result was compared to the measured I_{out}. The maximum difference in the estimated Θ_{in} at each step was less than $\pm 0.2\pi$.

Received 19 April 2010; accepted 20 July 2010; published online 29 August 2010

References

1. Icsevgi, A. & Lamb, W. E. Propagation of light pulses in a laser amplifier. *Phys. Rev.* **185,** 517–545 (1969).
2. Lamb, G. L. Analytical descriptions of ultrashort optical pulse propagation in a resonant medium. *Rev. Mod. Phys.* **43,** 99–124 (1971).
3. Nakazawa, M., Suzuki, K., Kimura, Y. & Kubota, H. Coherent π-pulse propagation with pulse breakup in an erbium-doped fiber waveguide amplifier. *Phys. Rev. A* **45,** R2682–R2685 (1992).
4. Zhang, J.-Z. & Galbraith, I. Rabi oscillations of ultrashort optical pulses in 1.55 μm InGaAs/InGaAsP quantum-well amplifiers. *J. Appl. Phys.* **96,** 922–924 (2004).
5. Wang, C. Y. *et al.* Coherent instabilities in a semiconductor laser with fast gain recovery. *Phys. Rev. A* **77,** 031802 (2007).
6. Mosseini, M. *et al.* Coherent optical pulse sequencer for quantum applications. *Nature* **461,** 241–245 (2009).
7. Rabi, I. I. On the process of space quantization. *Phys. Rev.* **49,** 324–328 (1936).
8. Gibbs, H. M. Incoherent resonance fluorescence from a Rb atomic beam excited by a short coherent optical pulse. *Phys. Rev. A* **8,** 446–455 (1973).
9. Binder, R., Koch, S. W., Lindberg, M., Peyghambarian, N. & Schafer, W. Ultrafast adiabatic following in semiconductors. *Phys. Rev. Lett.* **65,** 899–902 (1990).
10. da Silva, V. L. & Silberberg, Y. Photon echoes in an optical amplifier. *Phys. Rev. Lett.* **70,** 1097–1100 (1993).
11. Cundiff, S. T. *et al.* Rabi flopping in semiconductors. *Phys. Rev. Lett.* **73,** 1178–1181 (1994).
12. Hughes, S. Breakdown of the area theorem: carrier-wave Rabi flopping of femtosecond optical pulses. *Phys. Rev. Lett.* **81,** 3363–3366 (1998).
13. Giessen, H. *et al.* Self-induced transmission on a free exciton resonance in a semiconductor. *Phys. Rev. Lett.* **81,** 4260–4263 (1998).
14. Dynes, J. F., Frogley, M. D., Beck, M., Faist, J. & Phillips, C. C. AC stark splitting and quantum interference with intersubband transitions in quantum wells. *Phys. Rev. Lett.* **94,** 157403 (2005).
15. Mücke, O. D., Tritschler, T., Wegener, M., Morgner, U. & Kärtner, F. X. Signatures of carrier-wave Rabi flopping in GaAs. *Phys. Rev. Lett.* **87,** 057401 (2001).
16. Stievater, T. H. *et al.* Rabi oscillations of excitons in single quantum dots. *Phys. Rev. Lett.* **87,** 133603 (2001).
17. Schülzgen, A. *et al.* Direct observation of excitonic Rabi oscillations in semiconductors. *Phys. Rev. Lett.* **82,** 2346–2349 (2004).
18. Luo, C. W. *et al.* Phase-resolved nonlinear response of a two-dimensional electron gas under femtosecond intersubband excitation. *Phys. Rev. Lett.* **92,** 047402 (2004).
19. Khitrova, G., Gibbs, H. M., Kira, M., Koch, S. W. & Scherer, A. Vacuum Rabi splitting in semiconductors. *Nature Phys.* **2,** 81–90 (2006).
20. Gunter, G. *et al.* Sub-cycle switch-on of ultrastrong light–matter interaction. *Nature* **458,** 178–181 (2009).
21. Menyuk, C. R. & Talukder, M. A. Self-induced transparency modelocking of quantum cascade lasers. *Phys. Rev. Lett.* **102,** 023903 (2009).
22. Talukder, M. A. & Menyuk, C. R. Analytical and computational study of self-induced transparency mode locking in quantum cascade lasers. *Phys. Rev. A* **79,** 063841 (2009).
23. McCall, S. L. & Hahn, E. L. Self-induced transparency. *Phys. Rev.* **183,** 457–485 (1969).
24. Allen, L. & Eberly, J. H. *Optical Resonance and Two Level Atoms* (Dover, 1987).
25. Liu, H. & Capasso, F. *Intersubband Transitions in Quantum Wells: Physics and Device Application II* (Academic Press, 2000).
26. Choi, H. *et al.* Time-domain upconversion measurements of group-velocity dispersion in quantum cascade lasers. *Opt. Express* **15,** 15898–15907 (2007).
27. Choi, H. *et al.* Gain recovery dynamics and photon-driven transport in quantum cascade lasers. *Phys. Rev. Lett.* **100,** 167401 (2008).
28. Choi, H. *et al.* Time-resolved investigations of electronic transport dynamics in quantum cascade lasers based on diagonal lasing transition. *IEEE J. Quantum Electron.* **45,** 307–321 (2009).
29. Gordon, A. *et al.* Multimode regimes in quantum cascade lasers: from coherent instabilities to spatial hole burning. *Phys. Rev. A* **77,** 053804 (2008).
30. Wang, C. Y. *et al.* Mode-locked pulses from mid-infrared quantum cascade lasers. *Opt. Express* **17,** 12929–12943 (2009).

Acknowledgements

Studies at the University of Michigan and MIT were supported by US Army Research Office. The authors acknowledge support from the Center for Nanoscale System (CNS) at Harvard University (Harvard–CNS is a member of the National Nanotechnology Infrastructure Network, NNIN). The Nanoscale Science and Engineering Center (NERC) at Harvard University, funded by the National Science Foundation, is also gratefully acknowledged.

Author contributions

H.C. designed and performed the experiments. V.-M.G. and H.C. carried out modelling, simulations and interpretation of the measurement results. L.D. calculated the band structure and fabricated the sample. S.C., J.Z. and G.H. grew the sample wafer. F.C., F.X.K. and T.B.N. initiated the work, managed the project and interpreted the data. All authors discussed the results and commented on the manuscript.

Additional information

The authors declare no competing financial interests. Reprints and permission information is available online at http://npg.nature.com/reprintsandpermissions/. Correspondence and requests for materials should be addressed to F.X.K. and T.B.N.